

Light trapping design for low band-gap polymer solar cells

Stephen Foster^{1,*} and Sajeev John^{1,2}

¹Department of Physics, University of Toronto, 60 St. George Street, Toronto, ON M5S1A7, Canada

²Department of Physics, King Abdul-Aziz University, Jeddah, Saudi Arabia

*sfoster@physics.utoronto.ca

Abstract: We demonstrate numerically a 2-D nanostructured design for light trapping in a low band-gap polymer solar cell. Finite element method simulations are used to study the effect of varying nanostructure periodicity, height, and shape on active layer absorption. Maintaining a constant active layer thickness of 100nm we observe an enhancement in solar absorption of almost 40% relative to a planar cell. Improvements of this magnitude enable single-junction, low-band-gap cells to achieve power conversion efficiencies of 11.2% and perform competitively with even state-of-the-art tandem cells. Our design is also shown to significantly outperform tandem cells at off-normal angles of incidence.

©2014 Optical Society of America

OCIS codes: (040.5350) Photovoltaic; (050.0050) Diffraction and gratings; (350.6050) Solar energy; (050.5298) Photonic crystals.

References and links

1. Z. He, C. Zhong, X. Huang, W.-Y. Wong, H. Wu, L. Chen, S. Su, and Y. Cao, "Simultaneous enhancement of open-circuit voltage, short-circuit current density, and fill factor in polymer solar cells," *Adv. Mater.* **23**(40), 4636–4643 (2011).
2. X. Li, W. C. H. Choy, L. Huo, F. Xie, W. E. I. Sha, B. Ding, X. Guo, Y. Li, J. Hou, J. You, and Y. Yang, "Dual plasmonic nanostructures for high performance inverted organic solar cells," *Adv. Mater.* **24**(22), 3046–3052 (2012).
3. Z. He, C. Zhong, S. Su, M. Xu, H. Wu, and Y. Cao, "Enhanced power-conversion efficiency in polymer solar cells using an inverted device structure," *Nat. Photonics* **6**(9), 591–595 (2012).
4. J. You, L. Dou, K. Yoshimura, T. Kato, K. Ohya, T. Moriarty, K. Emery, C.-C. Chen, J. Gao, G. Li, and Y. Yang, "A polymer tandem solar cell with 10.6% power conversion efficiency," *Nat. Commun.* **4**, 1446 (2013).
5. S. Nam, J. Han, Y. R. Do, H. Kim, S. Yim, and Y. Kim, "Two-dimensional photonic crystal arrays for polymer:fullerene solar cells," *Nanotechnology* **22**(46), 465403 (2011).
6. A. Raman, Z. Yu, and S. Fan, "Dielectric nanostructures for broadband light trapping in organic solar cells," *Opt. Express* **19**(20), 19015–19026 (2011).
7. D. H. Wang, J. Seifert, J. H. Park, D.-G. Choi, and A. J. Heeger, "Efficiency increase in flexible bulk heterojunction solar cells with nano-patterned indium zinc oxide anode," *Adv. Energy Mater.* **2**(11), 1319–1322 (2012).
8. D.-H. Ko, J. R. Tumbleston, L. Zhang, S. Williams, J. M. DeSimone, R. Lopez, and E. T. Samulski, "Photonic crystal geometry for organic solar cells," *Nano Lett.* **9**(7), 2742–2746 (2009).
9. L. Chen, W. E. I. Sha, and W. C. H. Choy, "Light harvesting improvement of organic solar cells with self-enhanced active layer designs," *Opt. Express* **20**(7), 8175–8185 (2012), <http://www.opticsinfobase.org/oe/abstract.cfm?uri=oe-20-7-8175>.
10. J. R. Tumbleston, D.-H. Ko, E. T. Samulski, and R. Lopez, "Absorption and quasiguide mode analysis of organic solar cells with photonic crystal photoactive layers," *Opt. Express* **17**(9), 7670–7681 (2009).
11. K. S. Nalwa and S. Chaudhary, "Design of light-trapping microscale-textured surfaces for efficient organic solar cells," *Opt. Express* **18**(5), 5168–5178 (2010).
12. D. Duché, L. Escoubas, J.-J. Simon, C. Gourgon, C. Masclaux, Ph. Torchio, J. Le Rouzo, and F. Flory, "Photonic crystals for improving light absorption in organic solar cells," *Proc. SPIE* **8256**, 82561K (2012).
13. X. H. Li, W. E. I. Sha, W. C. H. Choy, D. D. S. Fung, and F. X. Xie, "Efficient inverted polymer solar cells with directly patterned active layer and silver back grating," *J. Phys. Chem. C* **116**(12), 7200–7206 (2012).
14. J. You, X. Li, F. X. Xie, W. E. I. Sha, J. H. W. Kwong, G. Li, W. C. H. Choy, and Y. Yang, "Surface plasmon and scattering-enhanced low-bandgap polymer solar cell by a metal grating back electrode," *Adv. Energy Mater.* **2**(10), 1203–1207 (2012).
15. I. Kim, D. S. Jeong, T. S. Lee, W. S. Lee, and K.-S. Lee, "Plasmonic nanograting design for inverted polymer solar cells," *Opt. Express* **20**(S5), A729–A739 (2012).

16. X. Li, W. C. H. Choy, X. Ren, J. Xin, P. Lin, and D. C. W. Leung, "Polarization-independent efficiency enhancement of organic solar cells by using 3-dimensional plasmonic electrode," *Appl. Phys. Lett.* **102**(15), 153304 (2013).
17. K. Forberich, G. Dennler, M. C. Scharber, K. Hingerl, T. Fromherz, and C. J. Brabec, "Performance improvement of organic solar cells with moth eye anti-reflection coating," *Thin Solid Films* **516**(20), 7167–7170 (2008).
18. W.-L. Min, A. P. Betancourt, P. Jiang, and B. Jiang, "Bioinspired broadband antireflection coatings on GaSb," *Appl. Phys. Lett.* **92**(14), 141109 (2008).
19. W. C. Luk, K. M. Yeung, K. C. Tam, K. L. Ng, K. C. Kwok, C. Y. Kwong, A. M. C. Ng, and A. B. Djuricic, "Enhanced conversion efficiency of polymeric photovoltaic cell by nanostructured antireflection coating," *Org. Electron.* **12**(4), 557–561 (2011).
20. T. Søndergaard, J. Gadegaard, P. K. Kristensen, T. K. Jensen, T. G. Pedersen, and K. Pedersen, "Guidelines for 1D-periodic surface microstructures for antireflective lenses," *Opt. Express* **18**(25), 26245–26258 (2010).
21. H. K. Raut, V. A. Ganesh, A. S. Nair, and S. Ramakrishna, "Anti-reflective coatings: A critical, in-depth review," *Energy Environ. Sci.* **4**(10), 3779–3804 (2011).
22. L. Dou, J. You, J. Yang, C.-C. Chen, Y. He, S. Murase, T. Moriarty, K. Emery, G. Li, and Y. Yang, "Tandem polymer solar cells featuring a spectrally matched low-bandgap polymer," *Nat. Photonics* **6**(3), 180–185 (2012).
23. G. Demésy, F. Zolla, A. Nicolet, M. Commandré, and C. Fossati, "The finite element method as applied to the diffraction by an anisotropic grating," *Opt. Express* **15**(26), 18089–18102 (2007).
24. P. Dular, C. Geuzaine, F. Henrotte, and W. Legros, "A general environment for the treatment of discrete problems and its application to the finite element method," *IEEE Trans. Magn.* **34**(5), 3395–3398 (1998).
25. E. D. Palik, *Handbook of Optical Constants of Solids* (Academic, 1998), Vol. I.
26. M. F. Al-Kuhaili, S. M. A. Durrani, and E. E. Khawaja, "Effects of preparation conditions and thermocoloration on the optical properties of thin films of molybdenum oxide," *Thin Solid Films* **408**(1–2), 188–193 (2002).
27. H. Hoppe, N. S. Sariciftci, and D. Meissner, "Optical constants of conjugated polymer/fullerene based bulk-heterojunction organic solar cells," *Mol. Cryst. Liq. Cryst.* **385**(1), 113–119 (2002).
28. J. You, C.-C. Chen, Z. Hong, K. Yoshimura, K. Ohya, R. Xu, S. Ye, J. Gao, G. Li, and Y. Yang, "10.2% power conversion efficiency polymer tandem solar cells consisting of two identical sub-cells," *Adv. Mater.* **25**(29), 3973–3978 (2013).
29. A. Naqavi, K. Söderström, F.-J. Haug, V. Paeder, T. Scharf, H. P. Herzig, and C. Ballif, "Understanding of photocurrent enhancement in real thin film solar cells: towards optimal one-dimensional gratings," *Opt. Express* **19**(1), 128–140 (2011).
30. S. Eyderman, S. John, and A. Deinega, "Solar light trapping in slanted conical-pore photonic crystals: Beyond statistical ray trapping," *J. Appl. Phys.* **113**(15), 154315 (2013).
31. L. J. Guo, "Nanoimprint lithography: methods and material requirements," *Adv. Mater.* **19**(4), 495–513 (2007).
32. S. Tawfick, M. De Volder, D. Copic, S. J. Park, C. R. Oliver, E. S. Polsen, M. J. Roberts, and A. J. Hart, "Engineering of micro- and nanostructured surfaces with anisotropic geometries and properties," *Adv. Mater.* **24**(13), 1628–1674 (2012).
33. K. S. Nalwa, J.-M. Park, K.-M. Ho, and S. Chaudhary, "On realizing higher efficiency polymer solar cells using a textured substrate platform," *Adv. Mater.* **23**(1), 112–116 (2011).
34. S. Biswas, O. Shalev, and M. Shtein, "Thin-film growth and patterning techniques for small molecular organic compounds used in optoelectronic device applications," *Annu. Rev. Chem. Biomol. Eng.* **4**(1), 289–317 (2013).
35. A. M. Coclite, R. M. Howden, D. C. Borrelli, C. D. Petruczuk, R. Yang, J. L. Yagüe, A. Ugur, N. Chen, S. Lee, W. J. Jo, A. Liu, X. Wang, and K. K. Gleason, "25th anniversary article: Cvd polymers: A new paradigm for surface modification and device fabrication," *Adv. Mater.* **25**(38), 5392–5423 (2013).
36. F. Monestier, J.-J. Simon, P. Torchio, L. Escoubas, F. Flory, S. Bailly, R. de Bettignies, S. Guillerez, and C. Defranoux, "Modeling the short-circuit current density of polymer solar cells based on P3HT:PCBM blend," *Sol. Energy Mater. Sol. Cells* **91**(5), 405–410 (2007).
37. Y. Zhou, C. Fuentes-Hernandez, J. W. Shim, T. M. Khan, and B. Kippelen, "High performance polymeric charge recombination layer for organic tandem solar cells," *Energy Environ. Sci.* **5**(12), 9827–9832 (2012).
38. L. A. A. Pettersson, S. Ghosh, and O. Inganäs, "Optical anisotropy in thin films of poly(3,4-ethylenedioxythiophene)-poly(4-styrenesulfonate)," *Org. Electron.* **3**(3-4), 143–148 (2002).
39. H. K. Raut, S. S. Dinachali, A. Y. He, V. A. Ganesh, M. S. M. Saifullah, J. Law, and S. Ramakrishna, "Robust and durable polyhedral oligomeric silsesquioxane-based anti-reflective nanostructures with broadband quasi-omnidirectional properties," *Energy Environ. Sci.* **6**(6), 1929–1937 (2013).

1. Introduction

Recent progress in polymer solar cell (PSC) research has been rapid, with power conversion efficiencies now reaching 8-9% in single junction cells [1–3] and 10.6% in tandem cells [4]. Despite this improvement, higher efficiencies will be required for PSCs to be viable in the highly competitive solar cell market. A fundamental limitation facing PSCs is the requirement that active layer thickness remain on the order of charge carrier diffusion lengths, typically ~100-300nm for bulk hetero-junction (BHJ) cells. Increasing the active layer thickness beyond this point leads to significantly increased charge recombination and degrades overall cell performance. However, thin active layers yield very low light harvesting efficiencies.

Many strategies have been considered for circumventing this tradeoff. One popular approach has been to incorporate highly ordered periodic nanostructures in the cell. The goal of such structures is to use wave optics or plasmonics to guide the flow of light and increase absorption without increasing active layer thickness. Periodic structures that have been investigated include diffraction gratings placed above the active layer of the cell [5–7], photonic crystals embedded within the active layer [8–10], and metallic back-contact gratings adjoining the active layer [2,11–16].

Nanostructured cells have been optically modeled using a variety of computational techniques, including finite-difference time-domain (FDTD) [2,12–15], rigorous coupled wave analysis (RCWA) [6], scattering matrix method (SMM) [9,10] and finite element method (FEM) [11]. Of these theoretical investigations, the highest reported enhancement in absorption relative to a planar cell is 40% [11]. However, the enhancement reported in this work was relative to a planar cell with an artificially thin active layer, and the enhancement dropped off sharply for off-normal angles of incidence. Also of note is that almost all studies of periodic nanostructures to date have used a standard high band-gap polymer (such as poly-(3-hexylthiophene), or P3HT) as an electron donor material. In this work we use a state-of-the-art low band-gap polymer as an active material, and demonstrate large enhancement relative to a planar cell with a full-thickness active layer, leading to a projected power conversion efficiency (PCE) of 11.2% over a wide range of incident angles.

Periodic nanostructures have also attracted attention for their anti-reflective properties. Wavelength- or subwavelength-scale structures can provide a graded effective refractive index that minimizes reflection at interfaces. Examples of designs that have been studied for use in solar cells include so-called “moth’s eye” structures [17], pyramidal/conical structures [18], nanospheres [19], and triangular corrugation [20]. Techniques for creating anti-reflective structures are reviewed in [21]. In this work we demonstrate the effectiveness of triangular corrugation for anti-reflection and study the effect of varying corrugation height and period at different angles of incidence.

Recently, there has been a great deal of progress in synthesizing low band-gap (LBG) polymers for use in high-efficiency single-junction and tandem cells [4,22]. This development has been the main factor behind the increase in tandem cell efficiencies to >10%. Most notable of the new LBG materials is the polymer poly[2,7-(5,5-bis-(3,7-dimethyl octyl)-5H-dithieno[3,2-b:2',3'-d]pyran)-alt-4,7-(5,6-di)uoro-2,1,3-benzothiadiazole] (PDTP-DFBT), which has a band gap of 1.38eV [22]. PDTP-DFBT absorbs over a broad spectral range but has relatively low charge carrier mobility, necessitating a thin active layer (~100nm). As a result solar absorption is incomplete (~70%) over the entire spectral range, making it an ideal material for targeting with light-trapping strategies. As PDTP-DFBT is a relatively new material, optical models can be of great utility in providing direction for future experimental studies.

In this paper we investigate numerically a cell with a 2-D trapezoidally structured metallic back-contact, similar to that of [11]. The active layer studied is a blend of PDTP-DFBT and [6,6]-phenyl C71-butyric acid methyl ester (PC₇₁BM). The cell is modeled optically in the frequency domain using a 2D formulation of the finite element method (FEM) [23], implemented in the getdp software package [24]. Absorption, reflection and transmission coefficients are calculated for wavelengths ranging from 350 to 1000nm with 2nm step sizes. Active layer absorption is calculated and integrated over the AM 1.5 solar spectrum to give the maximum allowable photocurrent density (MAPD). MAPD is studied as a function of nanostructure shape, periodicity and height, with active layer thickness kept fixed at 100nm. Triangular corrugation is added to the air-glass interface of the cell to minimize reflection losses, and optimal corrugation periodicity and height are investigated. An overall enhancement in MAPD of almost 40% is found, one the highest yet reported for a numerical study of PSCs. Enhancement is shown to be due to photonic crystal-based light trapping in the active layer. This may lead to single-junction organic solar cells with power conversion efficiencies exceeding 11%. Field intensities of over 50 times the incident intensity are

observed for certain photonic modes. Finally, the design is studied for off-normal angles of incidence and shown to outperform a state-of-the-art tandem cell.

2. Simulation setup

A diagram of the device architecture studied is shown in Fig. 1. From bottom to top the layers of the cell are: device substrate, Ag, MoO₃, PDTP-DFBT:PC₇₁BM, nanocrystalline ZnO (nc-ZnO), ITO, and glass. The substrate is given a periodic trapezoidal structure, with Ag, MoO₃ and PDTP-DFBT:PC₇₁BM layered conformally on top and nc-ZnO nanostructures filling in the remaining gaps. For most calculations in this paper Ag is used as a substrate material, for simplicity. Given the expensive nature of silver however, this would not be ideal for real-world cells, and so we also demonstrate the effectiveness of our design with just a thin conformal Ag layer, and a “substrate” of air beneath the cell. The geometry of the entire structure can be specified by defining the shape of the grating, using the periodicity (a), grating height (h), opening width (w_1) and bottom width (w_2). The thicknesses of the MoO₃, PDTP-DFBT:PC₇₁BM, and ITO layers are kept fixed at 15nm, 100nm, and 180nm, respectively. The thickness of the planar nc-ZnO layer above the nanostructures is also kept fixed at 50nm. When necessary the glass layer thickness is varied to average over any spurious thin film interference effects. Corrugation geometry is specified by the corrugation height (h_c) and corrugation periodicity (a_c). To avoid extensive use of supercell calculations, the corrugation periodicity is constrained to integer fractions of the grating periodicity (*i.e.* $a_c = a, a/2, a/3$, etc.).

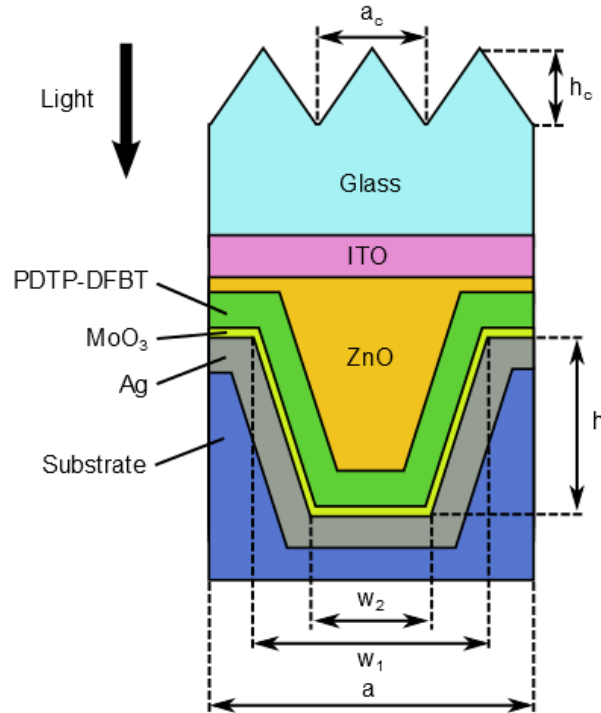


Fig. 1. Diagram of the cell structure studied in this work.

Incident light is treated as a TM-polarized plane wave (magnetic field transverse to plane of cell) with an angle of incidence θ . TM-polarization is chosen so that the electric field is polarized along the direction that the dielectric function varies. This is representative of what incident light would encounter in a real 3D cell (*i.e.* with a 2D square lattice geometry). Previous groups have found that 2D simulations with TM polarization give very similar results to comparable 3D simulations with square lattice geometries [10]. An FEM formulation, described in detail in [23], is used to solve for the electric field throughout the cell. Bloch boundary conditions are applied to the left and right of the cell, and perfectly

matched layers (PMLs) bound the computational domain above and below. Once the full electric field \mathbf{E} and the incident magnetic and electric fields \mathbf{H}_0 and \mathbf{E}_0 are known, the fraction of light absorbed by any given region of the cell can be calculated using:

$$\alpha_i(\lambda) = \frac{\int_{A_i} \omega \varepsilon_0 \Im(\varepsilon) |\mathbf{E}|^2 dx dy}{\int_S \Re\{\mathbf{E}_0 \times \mathbf{H}_0^*\} \hat{y} dx} \quad (1)$$

where ω is the frequency and ε is the complex-valued frequency-dependent dielectric function. The integrand in the numerator is the dielectric power loss density, which is integrated over a desired region of the cell, A_i , to obtain the absorbed power. Absorbed power is normalized to the incident power, calculated by integrating the y-component of the incident Poynting vector along a horizontal line above the cell, S . In this way we can calculate the fraction of light absorbed by each region of the cell separately. Reflection and transmission coefficients are calculated in a similar manner. These quantities are calculated for wavelengths ranging from 350nm to 1000nm in 2nm step sizes.

Knowing the fraction of incident power absorbed by the active material (denoted α_{act}) we calculate the maximum allowable photocurrent density (MAPD) using the equation:

$$J_{MAPD} = \int_{350\text{nm}}^{1000\text{nm}} \frac{e\lambda}{hc} I(\lambda) \alpha_{act}(\lambda) d\lambda \quad (2)$$

where e is the electron charge, λ is the vacuum wavelength, h is Planck's constant and c is the speed of light in a vacuum. $I(\lambda)$ is the AM 1.5 solar spectrum, assumed to be collimated in a TM-polarized beam with angle of incidence θ . MAPD assumes perfect charge collection – *i.e.*, that every absorbed photon generates one electric charge that contributes to the current.

Where possible, optical data for the materials studied was taken from the literature [8,25–27]. However, optical data for PDTP-DFBT:PC₇₁BM has not yet been published, and so was inferred from light harvesting efficiency data published in [28]. To extract the desired data, the cell described in that paper was simulated using our FEM code, and the imaginary part of the refractive index (k) for the PDTP-DFBT:PC₇₁BM layer was varied until the simulated absorption matched the measured absorption spectrum. The calculation was repeated for a range of wavelengths across the absorption spectrum. A value of 1.8 for the real part of the refractive index was assumed for this procedure. The procedure was repeated for a number of different glass thicknesses to average out spurious interference effects. The resulting data for k is shown in Fig. 2. By necessity this approach is approximate, but it is sufficient to allow for comparisons of absorption between geometries.

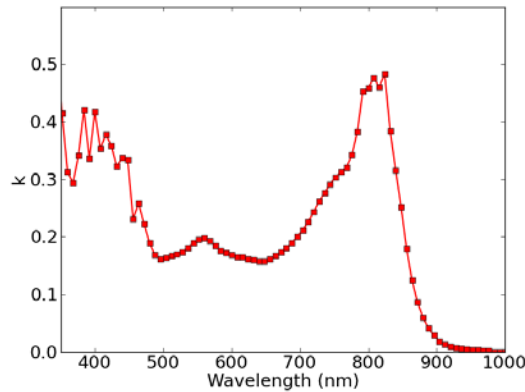


Fig. 2. Calculated values for the imaginary part of the refractive index (k) for PDTP-DFBT:PC₇₁BM. Obtained using absorption data from [28].

3. Results and discussion

For reference, we first calculate the MAPD for a cell with planar geometry. For this calculation cell layers from bottom to top are: silver (50nm thick), MoO₃ (15nm),

PDTP-DFBT:PC₇₁BM (100nm), nc-ZnO (30nm), ITO (180nm) and glass (variable thickness). An MAPD value of 21.96 mA/cm² is obtained. This value is used as a reference in characterizing our nanostructured design.

3.1 Grating shape

The first step in investigating our nanostructured design is to determine the optimal shape (*i.e.* opening width and bottom width) of the silver grating. For this we fix the periodicity a and structure height h at 1000nm each. Opening width w_1 is varied from $0.5a$ to a , and bottom width w_2 is varied from $0.2w_1$ to $0.8w_1$. With this we can study the full range of grating shapes, from square-like (w_1 close to w_2) to triangle-like (large w_1 and small w_2). No corrugation is present at the glass-air interface for these calculations.

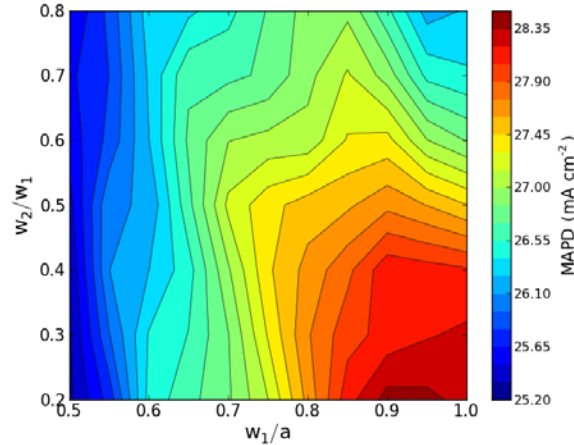


Fig. 3. Map of MAPD as a function of opening width w_1 and bottom width w_2 of the grating. Triangular-shaped gratings yield the best performance.

Figure 3 shows MAPD as a function of w_1 and w_2 . Absorption is highest for $w_1 = 0.96a$ and $w_2 = 0.2w_1$, corresponding to a triangle-like structure. Similar results were found for other grating periodicities and heights. To our knowledge this is the first optimization of grating shape in PSCs with conformal active layers. Naqavi et al. studied conformal thin-film silicon cells and also found triangular gratings to be most effective [29]. We adopt the values $w_1 = a$ and $w_2 = 0.2w_1$ for all subsequent calculations.

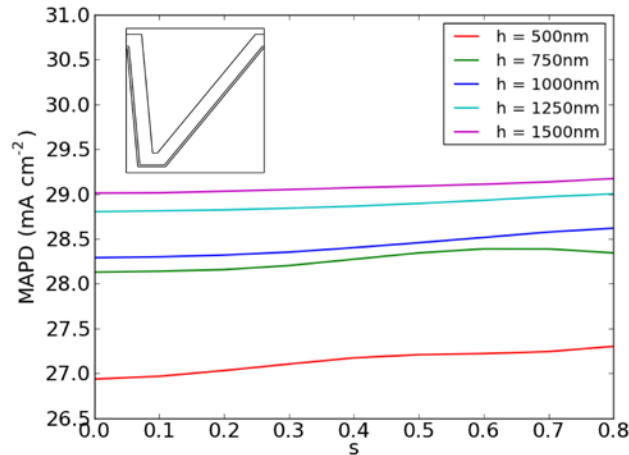


Fig. 4. MAPD for different values of h as a function of the slant factor s . A value of $s = 0$ corresponds to no slant, and $s = 1$ corresponds to a fully slanted sawtooth shape. Inset shows grating geometry for $h = 1000\text{nm}$ and $s = 0.8$.

Several groups have found that introducing asymmetry to nanostructured cells can improve performance [29,30]. To determine if this is true for our design, we apply a slant to

the grating structure. This is done by shifting the lower part of the grating to one side while the upper part is held fixed. The values for w_1 and w_2 are kept constant, and all layers are maintained as conformal with the same layer thicknesses. We define a linear slant factor s to characterize the asymmetry, where $s = 0$ corresponds to a symmetric design, and $s = 1$ corresponds to a fully asymmetric design with one of the grating walls being perfectly vertical (*i.e.*, a sawtooth-like shape). The inset of Fig. 4 shows an example geometry with $s = 0.8$. We again choose $a = 1000\text{nm}$ and look at a range of values for h , from 500nm to 1500nm . Figure 4 shows MAPD as a function of s for the different grating heights. In all cases MAPD increases as asymmetry is introduced; however, the overall increase is quite small ($\sim 0.2\text{mA}/\text{cm}^2$). Our design seems to be relatively insensitive to asymmetry. Due to the small performance improvement obtained we simply set $s = 0$ for subsequent calculations.

3.2 Grating period and height

Figure 5(a) shows MAPD as a function of grating periodicity and height. Periodicity is varied from 400nm to 1400nm , and grating height from 350nm to 2000nm . The data show a trend towards higher MAPD for larger grating heights and for shorter periodicities. This is primarily due to the presence of more active material per unit area as the aspect ratio of the structures is increased. Note that this increase in active material volume does not correspond to increased travel distances for photo-generated charges, as the active layer thickness is kept constant.

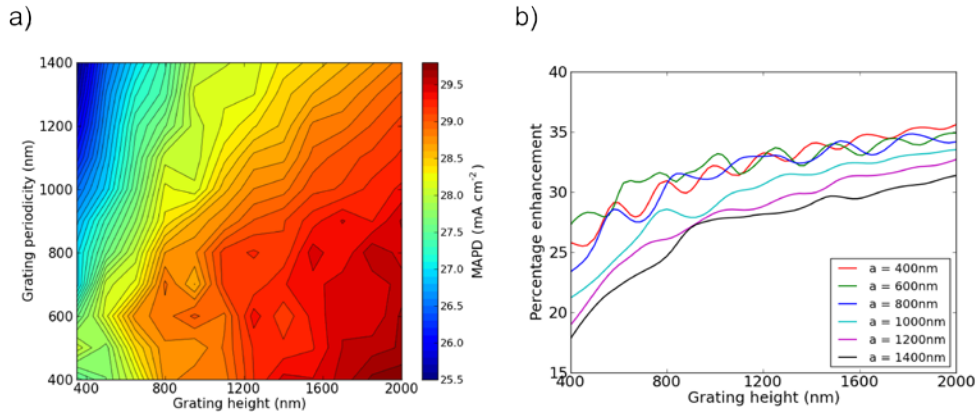


Fig. 5. (a) Map of MAPD as a function of the grating periodicity a and grating height h . (b) The same data expressed in terms of enhancement in MAPD relative to the reference planar cell. High aspect ratio gratings yield the largest improvement.

Figure 5(b) shows enhancement in MAPD relative to the planar cell as a function of grating height, for select periodicities. It is difficult to quote a single enhancement factor, as device enhancement could in principle be increased indefinitely by continuing to increase the grating height. It might be expected that increasing the grating height in this manner would eventually lead to poor performance at off-normal angles of incidence. However, this was found not to be the case: MAPD continued to increase with grating height regardless of incident angle, up to a grating height of $3.5\mu\text{m}$ (the highest studied). We found no evidence for an optimal grating height from a light harvesting perspective. However, the geometry of a real-world cell of this design would depend on a number of additional factors: manufacturing capabilities, electrical performance, material costs, etc. For practical purposes, we restrict grating height and periodicity to less than two microns. This is approximately the largest feature size reported with nano-imprint lithography [31,32]. We highlight a few geometries for illustration: the high aspect ratio cell with $a = 400\text{nm}$ and $h = 2000\text{nm}$ yields an enhancement of 35%, the highest of any geometry studied. A lower aspect ratio structure with $a = 800$ and $h = 1600$ yields a slightly reduced enhancement of 33%. The sub-micron grating

with wavelength-scale features ($a = 600\text{nm}$ and $h = 600\text{nm}$) enables a 30% enhancement. However, some authors have suggested that low-aspect ratio structures with large periodicities (1 micron or greater) more easily allow for a conformal coating of active material [33]. In this case, our design still provides enhancements of over 20% (e.g., with $a = 1200\text{nm}$ and $h = 500\text{nm}$).

Some of the observed enhancement shown by our design is simply due to the higher volume of active material that is permitted by having a conformal active layer. However, a significant fraction of the enhancement can be attributed to photonic crystal light trapping. To quantify this we calculate MAPD as a function of *equivalent thickness*; i.e., the active layer thickness the cell would have if all active material were redistributed into a planar slab. This ensures that only cells with the same amount of active material are directly compared, allowing us to isolate the role of light-trapping. MAPD is plotted versus equivalent thickness in Fig. 6 for several periodicities. Also shown for reference is MAPD for the planar geometry cell as a function of active layer thickness. In general the patterned cells significantly outperform the planar cell for equivalent thicknesses less than 300 nm. We conclude that light-trapping plays a significant role in thin-active-layer solar cells. Above approximately 500nm equivalent thickness, the patterned cells and planar cell perform roughly the same. A key feature of our photonic crystal design (with conformal active layer) is that it enables equivalent thicknesses beyond the typical diffusion length of photo-generated carriers. For a planar cell, the active layer thickness cannot be more than $\sim 120\text{nm}$ without significantly degrading electrical performance [28].

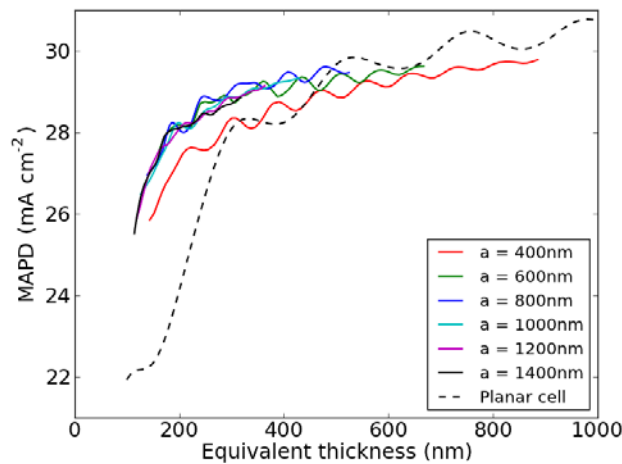


Fig. 6. MAPD for different grating periodicities as a function of equivalent thickness of the active layer. Dashed line shows planar cell MAPD as a function of active layer thickness.

Finally, we consider a specific geometry with high performance ($a = 800\text{nm}$ and $h = 1600\text{nm}$) for more detailed analysis. A breakdown of energy losses in the cell is plotted in Fig. 7 as a function of wavelength. A high percentage of incident light is absorbed by the active material, with losses split between parasitic absorption by other materials, and reflection. The dotted line shows active layer absorption for the planar cell. The structured cell outperforms the planar cell by a significant margin for essentially all wavelengths. To understand the source of this enhancement we look at the field profile within the cell. Figure 8(a) shows maps of the electric field intensity $|E|^2$ and time-averaged Poynting vector within the cell, for incident wavelengths of 600nm and 930nm. At 600nm we see a maximum intensity enhancement of 4.3 (relative to the incident intensity), concentrated in the upper portion of the MoO_3 layer. The Poynting vector map shows that as energy enters the cell it is directed out of the low-index nc-ZnO region ($n \sim 1.5$), into the 100 nm active layer ($n = 1.8$) and thin 15 nm MoO_3 layer ($n \sim 2.1$) where wave-guiding takes place. Index guiding of this

type is observed for a wide range of wavelengths (roughly 450-850nm). The field intensity and Poynting vector distributions for these wavelengths all show patterns similar to the 600nm case shown.

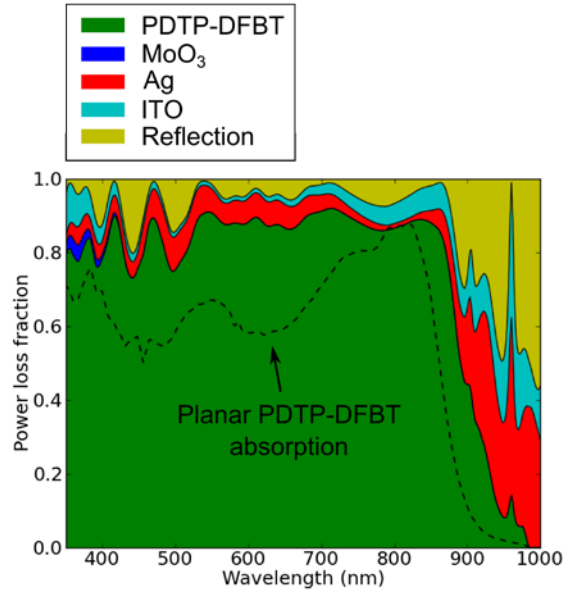


Fig. 7. Breakdown of energy losses within the cell as a function of wavelength for $a = 800\text{nm}$ and $h = 1600\text{nm}$. Active layer absorption for planar reference cell shown as dashed line.

For wavelengths in the range of 850-1000nm, more complicated photonic modes were observed. These were characterized by intensity distributions that showed a number of highly localized regions of very strong enhancement (greater than 50 times incident field intensity in some cases) within the MoO_3 and active layer regions of the cell. A wavelength of 930nm is highlighted in Fig. 8(b). Both the intensity distribution and Poynting vector field show considerably more structure than in the shorter-wavelength case above. Vorticity in the Poynting vector field can be seen at the center of the image, and is observed for the entire wavelength range in question. This circulation of energy flow leads to enhanced dwell time of light in the active layer and increases absorption. Similar vortex-like patterns have been observed in theoretical studies of thin-film conical-pore silicon solar cells [30]. Although Nalwa *et al.* [11] report an index guiding effect similar to what we observe at shorter wavelengths, their design does not take advantage of these high-intensity photonic modes for light-trapping at longer wavelengths, as ours does.

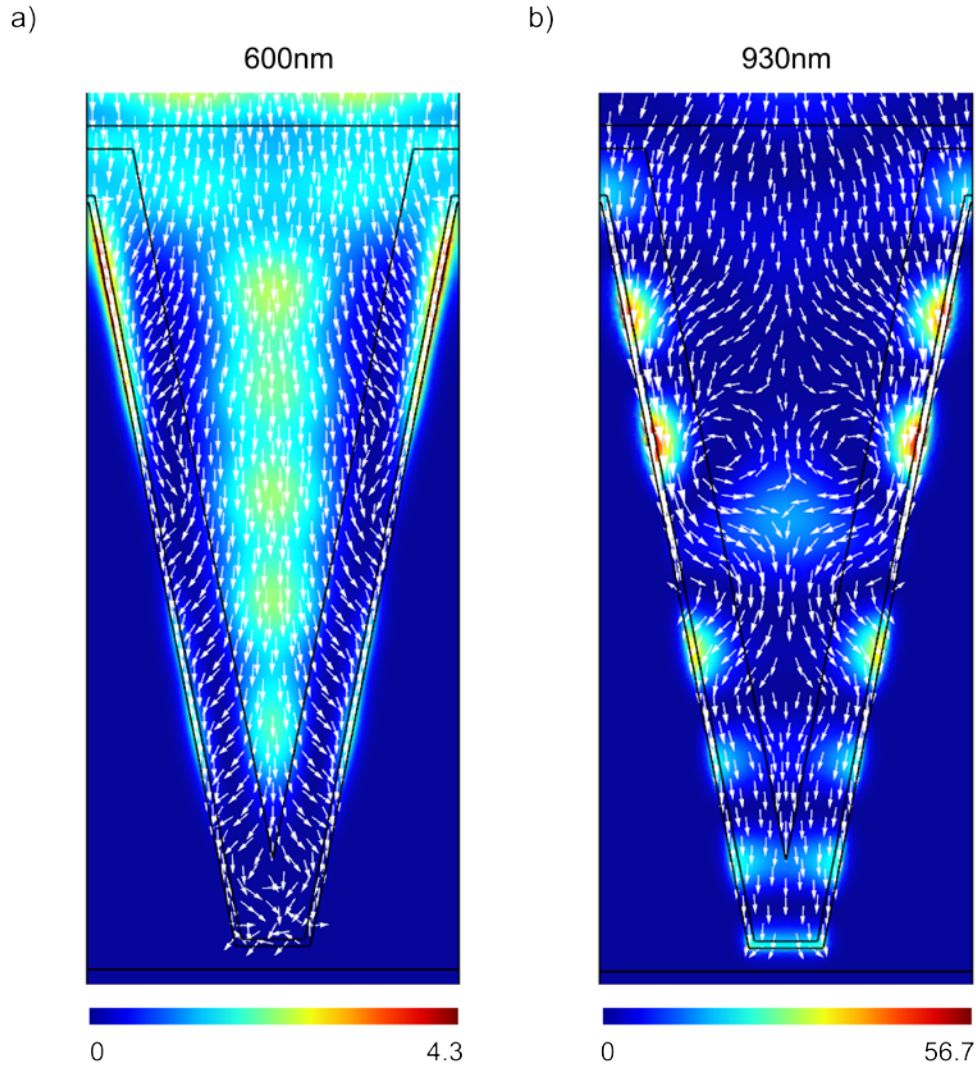


Fig. 8. Map of electric field intensity $|E|^2$ (normalized to incident intensity) and time-averaged Poynting vector for a cell with $a = 800\text{nm}$ and $h = 1600\text{nm}$, for incident wavelengths of a) 600nm and b) 930nm .

3.3 Triangular corrugation

Typical reflection losses for the above calculations are in the range of 5-10%. This leaves room for significant absorption enhancement with an anti-reflective layer in place. In this work we consider a simple triangular corrugation of the glass-air interface of the cell, defined by a period a_c and height h_c . Corrugation periods of $a_c = a$, $a/2$, $a/3$ and $a/4$ are studied; only integer fractions of a are considered so as to avoid the need for supercell calculations. To find the optimal values for h_c and a_c , grating height is fixed at $h = 800\text{nm}$ (see Fig. 1), and the corrugation height h_c is varied from 0nm to 700nm for each of the four corrugation periodicities. Values for a of 600nm , 900nm and 1200nm are considered, giving a total of 12 curves.

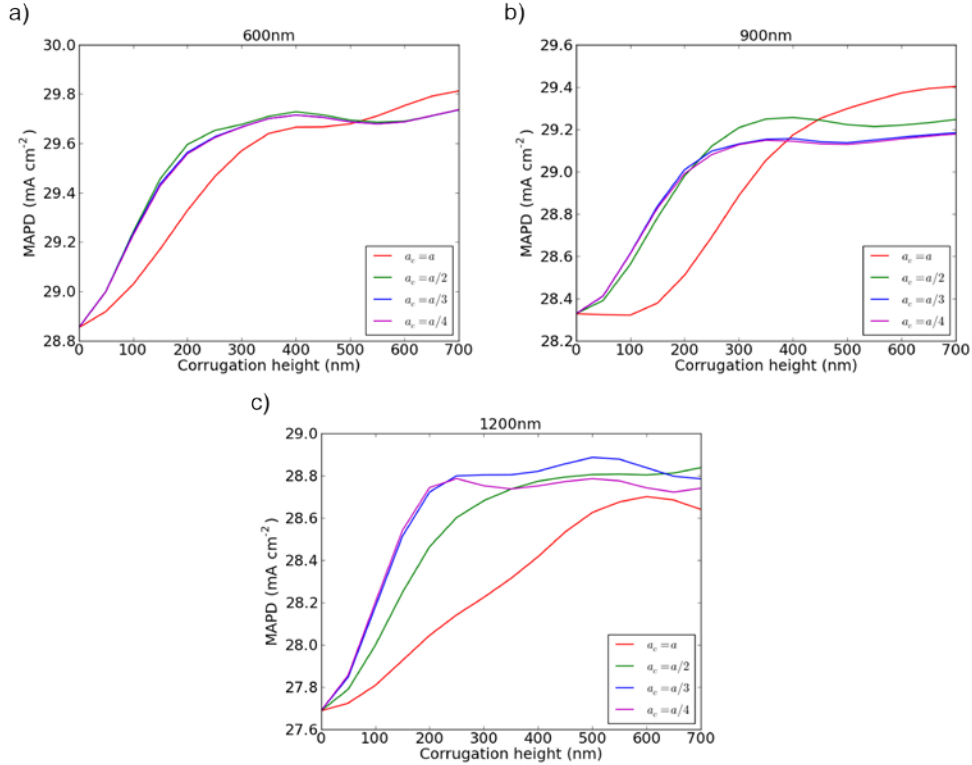


Fig. 9. MAPD as a function of corrugation height h_c for $a_c = a, a/2, a/3$ and $a/4$. Results are shown for (a) $a = 600\text{nm}$, (b) $a = 900\text{nm}$ and (c) $a = 1200\text{nm}$. Grating height is fixed at $h = 800\text{nm}$ (see Fig. 1).

Results are shown in Fig. 9. For all cells MAPD follows a similar trend, increasing with corrugation height initially before reaching a plateau. Most cells see a maximum improvement in MAPD of $\sim 1\text{mA}/\text{cm}^2$. There is some indication from the data that wavelength-scale corrugation periodicities ($a_c = 300\text{-}1000\text{nm}$) tend to yield the highest performance. A possible explanation for this is that wavelength-scale corrugation transmits light into higher diffractions orders (as noted in, *e.g.*, [20]), in effect acting as both an anti-reflective layer and diffraction grating. However, the effect is a small one.

In determining the ideal corrugation period it is important to consider performance at oblique angles of incidence. Most polymer solar cells are not fitted with sun tracking devices, and so receive much of their solar irradiation from off-normal angles. We look at MAPD for the same three grating periodicities and four corrugation periods as a function of angle of incidence, with h_c set to 700nm . Results are shown in Fig. 10. Data for $a_c = a/3$ is not shown to minimize visual clutter; MAPD is similar to that observed for $a_c = a/4$. Off-normal performance is very good overall, with a roughly constant or slightly increasing MAPD observed for all periodicities out to a 60° angle of incidence. Averaging over all angles the best performance is given by a corrugation period of $a_c = a/4$, and so that value is adopted for subsequent calculations. As noted above, however, the performance differences for different values of a_c are relatively small, indicating that the anti-reflective properties of corrugation are not very sensitive to periodicity.

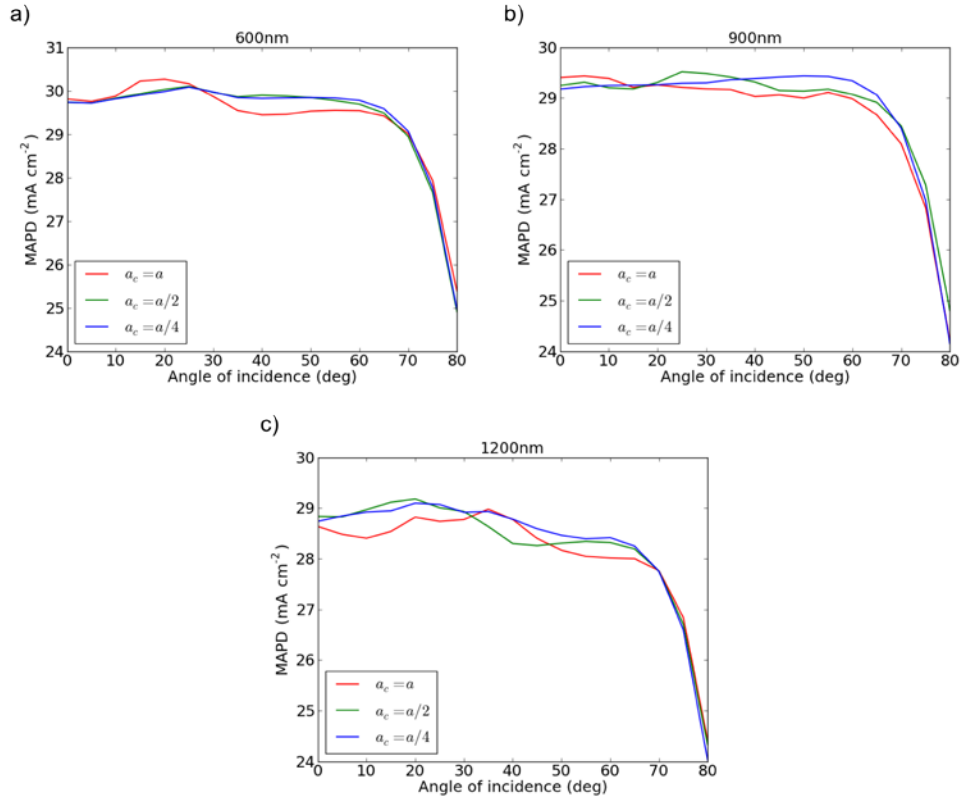


Fig. 10. MAPD as a function of angle of incidence for the corrugation periodicities $a_c = a$, $a/2$, and $a/4$. Results are shown for grating periodicities of (a) 600nm, (b) 900nm and (c) 1200nm. Grating height is fixed at $h = 800\text{nm}$ (see Fig. 1).

With corrugation in place we again calculate MAPD as a function of grating height and grating periodicity. For concreteness we set $h_c = 700\text{nm}$, although values as small as 200nm would be nearly as effective. Figure 11(a) shows enhancement in MAPD relative to planar cell as a function of h , for select values of a . Comparing with enhancements reported in Fig. 5(b) above we see noticeable improvements. For example, for a cell with $a = 400\text{nm}$ and $h = 2000\text{nm}$ we now see an enhancement of 40%; this is again the highest performing geometry. With $a = 800\text{nm}$ and $h = 1600\text{nm}$ an enhancement of 38% is obtained. A cell with $a = 600\text{nm}$ and $h = 600\text{nm}$ now gives an enhancement of 33%, and a cell with $a = 1200\text{nm}$ and $h = 500\text{nm}$ now shows a 25% enhancement. These are among the largest reported enhancements for nanostructured PSCs that persist over a wide range of incident angles.

To examine wavelength dependence we again use the cell with $a = 800\text{nm}$ and $h = 1600\text{nm}$. Figure 11(b) gives a breakdown of the energy balance for this cell as a function of wavelength. The addition of the anti-reflective layer sharply reduces reflection losses across all wavelengths. This leaves parasitic absorption by the ITO and silver layers as the main source of loss in the cell. An impressive 80% of all incident photons from 350 to 1000nm are absorbed by the active material. Active layer absorption for the planar cell (dotted line) is much lower, amounting to only 58% of incident photons absorbed.

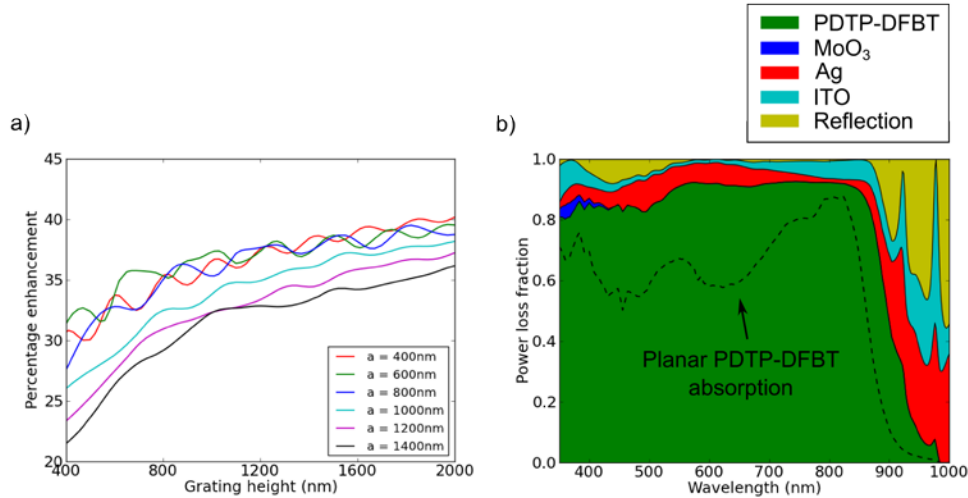


Fig. 11. (a) Enhancement in MAPD relative to planar cell as a function of grating height for select periodicities. Triangular corrugation with $a_c = a/4$ and $h_c = 700\text{nm}$ is applied at the glass-air interface. (b) Breakdown of energy losses for cell with $a = 800\text{nm}$ and $h = 1600\text{nm}$. Dashed line shows active layer absorption for planar reference cell.

3.4 Real world considerations

The most likely manufacturing procedure for our design would be as follows: deposition of the glass, ITO, and ZnO layers, followed by nanoimprinting of the ZnO layer, followed by deposition of the active layer, MoO₃ and Ag. All calculations to this point have considered a cell with a bulk layer of Ag as a substrate material (see Fig. 1). However, overfilling the grating with Ag in this manner would be costly. To demonstrate that this volume of Ag is not needed to obtain high performance, we consider a cell with just a thin conformal Ag layer, and air beneath the cell. Setting $a = 800\text{nm}$ and $h = 1600\text{nm}$ we calculate MAPD as a function of Ag layer thickness. Results are shown in Fig. 12(a). MAPD quickly asymptotes as the Ag layer thickness is increased. With a layer thickness of 80nm, MAPD is only 0.4% below the MAPD obtained with a bulk Ag layer.

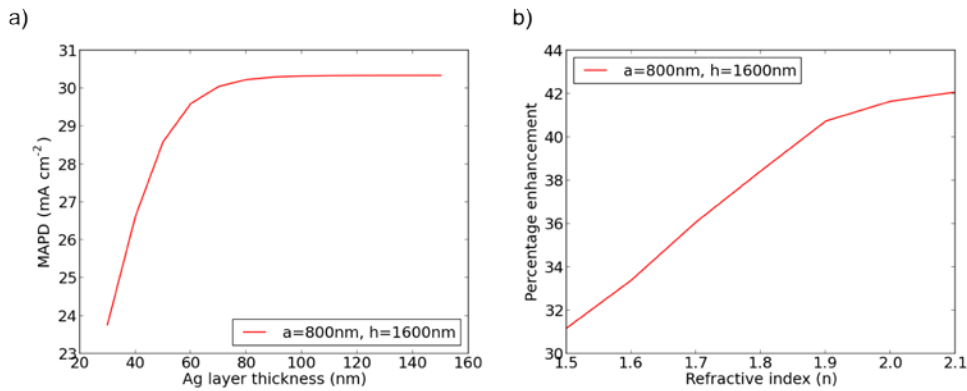


Fig. 12. (a) MAPD for a cell with a conformal Ag layer and air beneath the cell, as a function of Ag layer thickness ($a = 800\text{nm}$, $h = 1600\text{nm}$). (b) Percentage enhancement in MAPD for nanostructured cell ($a = 800\text{nm}$, $h = 1600\text{nm}$) relative to planar cell, as a function of active layer refractive index (n). The imaginary part of the index (k) is recomputed for each value of n using the procedure described in Sec. 2.

A prerequisite for implementing our design in real-world cells is the ability to deposit conformal layers of active material. At present this is challenging; however, promising steps are being made in this direction. Conformal deposition is already possible using standard spin-coating techniques in the case of low aspect ratio nanostructures [33]. In addition, in small-molecule organic solar cells the active layer is typically created using a solvent-free deposition technique, such as thermal evaporation [34]. Such techniques lend themselves readily to conformal layers. Our design could therefore be applied immediately to such cells. Finally, there has been recent work on using oxidative chemical vapour deposition (oCVD) to create active layers consisting of large polymers in PSCs [35], although this approach is limited to creating bilayer heterojunction cells. Vapour-based deposition techniques like this would allow for conformal layers of active material.

A final consideration is the dependence of device performance on the refractive index of the active material (PDTP-DFBT:PC₇₁BM). To this point we have assumed a constant refractive index of 1.8 for the active layer in lieu of experimental data. It is important to ensure that our results do not change significantly if different values for the refractive index are assumed. To verify this we considered our standard cell geometry of $a = 800\text{nm}$ and $h = 1600\text{nm}$, and varied the refractive index value from 1.5 to 2.1. This was deemed to be a reasonable range as it is similar to the index range for a few known polymer solar cell active materials (e.g. ~ 1.6 to 2.1 for P3HT:PC₇₀BM [36], ~ 1.7 to 2.2 for P3HT:ICBA [37], and ~ 1.8 to 2.3 for PBDTTT:PC₆₀BM [37]). For all cases we assume that the refractive index is constant. This is likely not the case for our active material, since it is highly absorbing over the wavelength range in question. However, as long as the variation in the index value is within the range of constant values studied here, cell performance can be estimated by combining results from constant index simulations. For each value of n , the imaginary part of the index k was recomputed using the procedure described in Sec. 2. MAPD was then calculated as a function of n for both planar and nanostructured geometries. Figure 12(b) shows percentage enhancement in MAPD relative to the planar cell as a function of n . Enhancement is not independent of n , ranging from 31% for $n = 1.5$ to 42% for $n = 2.1$. It is worth emphasizing that the 31% improvement corresponds (roughly speaking) to a material with an *average* index value of 1.5, which would be fairly low for a polymer of this type. However, even in this case the enhancement is still significant. Our design is relatively robust with respect to changes in the refractive index.

3.5 Comparison with tandem cell

The planar cell we have used as a reference has a real-world efficiency of 8.1% [28]. To give a projected efficiency for a cell with our design we assume that open-circuit voltage and fill factor values remain unchanged from real-world planar cell values, and that short-circuit current density is simply scaled up by our MAPD enhancement factor. These are reasonable assumptions given that active layer thickness is the same in both cells. In fact, fill factor values are typically found to *increase* with the introduction of nano-structuring [7,13,16], due to higher interfacial area between active layer and electrode, which both lowers the cell series resistance and allows for better charge collection. With these assumptions, for a cell with $a = 800\text{nm}$ and $h = 1600\text{nm}$, our design has a projected efficiency of 11.2%. This is well beyond the current record efficiency for single junction PSCs, and comparable to the highest tandem cell efficiencies.

Another advantage of our design is excellent performance at oblique angles of incidence. In contrast, the current matching requirement of tandem cells can lead to poor off-normal performance. To demonstrate this we simulate the 10.6% efficient cell of Yang *et al.* using our finite element method. Layers of the simulated cell from bottom to top are: Ag (50nm), MoO₃ (15nm), PDTP-DFBT:PC₇₁BM (100nm), ZnO (30nm), PEDOT:PSS (40nm), P3HT:ICBA (275nm), ZnO (30nm), ITO (180nm), and glass (1 μm). ICBA refers to Indene-C₆₀ Bisadduct, an electron acceptor. Optical data for PEDOT:PSS and P3HT:ICBA are taken from the literature [37, 38]. Yang's cell has a P3HT:ICBA layer thickness of 220nm; this is adjusted upwards here to 275nm to give matching MAPD values for the two active layers at

normal incidence. The matched MAPD value is $12.6\text{mA}/\text{cm}^2$. We simulate the tandem planar cell and our nanostructured cell for incident angles from 0 to 80° . MAPD is plotted in Fig. 13(a) for the nanostructured cell and the two active layers of the tandem cell, normalized to values at normal incidence. MAPD stays roughly constant for the nanostructured cell out to an incident angle of 60° . For the tandem cell, current matching is lost immediately as the angle of incidence is increased from zero, with MAPD increasing for the P3HT:ICBA layer and decreasing for the PDTP-DFBT:PC₇₁BM layer. Since it is a serially connected cell, performance is determined by the lower of the two active layer MAPD values. As a result our design outperforms the tandem cell at off-normal angles of incidence by an even wider margin than at normal incidence.

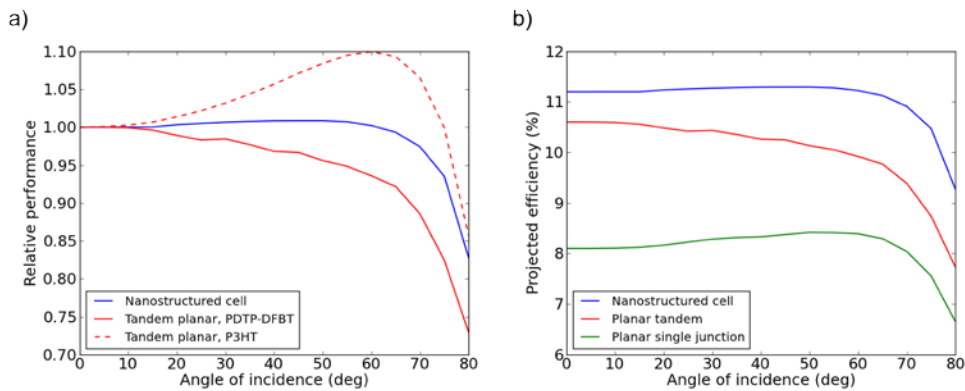


Fig. 13. (a) Relative change in MAPD as a function of angle of incidence for the nanostructured cell ($a = 800\text{nm}$, $h = 1600\text{nm}$) and a high-efficiency planar tandem cell. Data for both subcells of the tandem cell are shown. The lower of the two curves determines overall device performance. (b) Projected power conversion efficiencies for the nanostructured, single-junction planar and tandem planar cells as a function of angle of incidence, based on relative change in MAPD.

Finally we calculate projected efficiencies as a function of angle for the nanostructured cell, single junction planar cell and tandem planar cell. To do this we assume that efficiencies for the three cells at normal incidence are 11.2%, 8.1% and 10.6%, respectively (the latter two being experimental values, and the former based on 38% MAPD enhancement). These numbers are then scaled to match the relative change in MAPD for each cell as angle of incidence is varied. Results are plotted in Fig. 13(b). The nanostructured cell has a significantly higher projected efficiency than the two planar cells at all angles of incidence. Performance does not drop off significantly until angles of incidence above 70° are reached. This can be compared with the design shown in [11], for which performance drops above a 20° angle of incidence.

4. Conclusions

Using finite element method simulations we demonstrated the effectiveness of a nanostructured metallic grating for increasing light absorption in low band-gap PSCs. Triangular-shaped gratings were found to be the most effective shape for producing enhancement in absorption relative to a planar cell. Introducing asymmetry to the grating shape was found to have no significant effect. Absorption enhancement was due to both the presence of additional active material and photonic crystal light-trapping effects. Our results show that triangular corrugation at the air-glass interface can provide effective anti-reflection across the entire spectral range of incident light. Corrugation periodicities of 400nm or less were found to be the best choice when off-normal angles of incidence were taken into account. Although in our design the glass layer is itself corrugated, a similar effect could be achieved by creating a separate, nanostructured thin film and applying it on top of the glass layer, as in [39]. Final absorption enhancement relative to the planar cell ranged from 25 to

40% for the cell geometries studied, some of the largest enhancements reported yet for PSCs. Enhancements of this order would allow single-junction cells to compete with even the highest efficiency tandem PSCs. Our design was also found to have superior performance to tandem cells at oblique angles of incidence. Most importantly, our design employs a conformal active layer of the same thickness as that of the reference planar cell. This means the enhancements reported here could be realized without any compromise of the electrical properties of the cell, an essential feature for any proposed light-trapping scheme.

The grating structure we propose could be manufactured inexpensively using nano-imprinting techniques [31,32]. This could be applied to the ZnO layer and followed by conformal deposition of PDTP-DFBT:PC₇₁BM, MoO₃ and Ag. While conformal deposition of polymeric active layers on high-aspect-ratio structures is challenging, we present a few plausible pathways towards its achievement. We hope that our work demonstrating the excellent potential of photonic crystal, low-band-gap, PSCs may spur further development in the required process technologies.

Acknowledgments

The authors would like to thank Guillaume Demesy for his assistance with the FEM code. This work was supported in part by the United States Department of Energy under contract DE-FG02-10ER46754, the Canadian Institute for Advanced Research, and the Natural Sciences and Engineering Research Council (NSERC). Stephen Foster is also grateful to NSERC for a postgraduate scholarship.